(Received 14 June 2024, Accepted 15 July 2024, Scheduled 24 July 2024)

A 12-Unit Asymmetric Mirror-Coupled Loop Antenna for 5G Smartphones

Wanying Ren[1], Zhonggen Wang[1], Wenyan Nie[2,*], Weidong Mu[3], Chenlu Li[4], Mingqing Wang[1], and Wenshi You[1]

[1]*School of Electrical and Information Engineering, Anhui University of Science and Technology, Huainan 232001, China*
[2]*School of Mechanical and Electrical Engineering, Huainan Normal University, Huainan 232001, China*
[3]*School of Electronic and Information Engineering, Nanjing University of Aeronautics and Astronautics, Nanjing 211106, China*
[4]*School Electrical and Information Engineering, Hefei Normal University, Hefei 230061, China*

ABSTRACT: This paper introduces a 12-element asymmetric mirror-coupled loop antenna for integration into 5G smartphones. The proposed antenna includes six identical asymmetrically mirrored (AM)-coupled building blocks, each consisting of two gap-coupled loop antennas, with each building block dimensioning a mere $12 \times 7\,\text{mm}^2$. The unique architecture of the proposed antenna yields an isolation performance exceeding 14 dB without the necessity for ancillary decoupling elements and effectively covers the dual-band 5G mobile frequency bands of 3.3–3.6 GHz and 4.8–5.0 GHz. The antenna was optimized using simulation software HFSS, and the results indicate an antenna's envelope correlation coefficient of less than 0.016 and an efficiency range of 72%–81%. Finally, the performance of single-hand and double-hand handset smartphone modes is discussed, which still exhibit good radiation and MIMO performance under both modes, demonstrating their stability in practical applications. Simulation and measurement results indicate that the proposed 12-element MIMO antenna holds great promise for 5G smartphone applications.

1. INTRODUCTION

In 2017, the Ministry of Industry and Information Technology of China designated the 3.5 GHz (3.3–3.6 GHz) and 4.9 GHz (4.8–5.0 GHz) frequency bands as the 5G communication frequency bands. It is certain that multiple-input-multiple-output (MIMO) remains one of the key technologies applied in 5G systems [1]. However, the limited space on mobile phone substrates necessitates integrating multiple antennas, driving the trend towards incorporating antennas into the phone's frame. Yet, encasing traditional built-in antennas within a metal frame can compromise their performance. Moreover, accommodating the multi-frequency characteristics of mobile phone antennas poses considerable challenges for mobile antenna engineers. Consequently, there is a pressing demand for the design of frame antennas capable of covering the 5 GHz frequency bands.

Numerous scholars have proposed literature on 5G mobile frame antennas [2–15]. Antenna designs presented in [16, 17] could only cover the 3.4–3.6 GHz frequency band. The antenna proposed in [18] could operate in two frequency bands, namely 3.5 GHz band (3.4–3.6 GHz) and the 5 GHz band. The antenna in [19] achieved the 3.3–5 GHz frequency band by using coupled feed on the two long edges but is not suitable for 5G metal frame phones. The antenna designed in [20] was suitable for 5G metal frame phones but had a narrow bandwidth. The antenna in [21] was suitable for metal frame phones and could cover the 3.3–6 GHz band through direct feeding, but its 3 mm ground clearance was relatively large, resulting in larger overall dimensions for MIMO antennas.

These systems demonstrate advantages in isolation, while proposing and studying different technologies and decoupling structures to improve isolation. A new spatially multiplexed dual-antenna MIMO structure, known as antenna pairs [22, 23], has been recently studied. To decouple antenna pairs, most antennas utilize the elimination of resonant mode currents in shared radiators [24, 25], while some antennas leverage the polarization orthogonality of two antennas [26, 27]. Isolation structures in [28] achieved self-decoupling through orthogonal mode isolation, parasitic structures, polarization diversity, and structures based on mode elimination methods. Refs. [29–31] achieved high-isolation result by loading antenna pairs decoupled by aggregate elements.

Based on the above issues, this paper proposes a 12-unit asymmetric mirror-coupled loop antenna for 5G smartphones. The antenna consists of six identical AM coupling building blocks, each composed of two gapped-coupled ring antennas. These two antennas have an AM structure relative to the smartphone ground plane. Due to the antenna's unique structure, the proposed antenna achieves excellent isolation without the need for additional decoupling structures, with isolation greater than 14 dB. Additionally, simulated performances of the proposed antenna design in single-handed and two-handed smartphone modes during data transmission demonstrate that the MIMO antenna system meets the requirements of 5G communication.

* Corresponding author: Wenyan Nie (wynie5240@163.com).

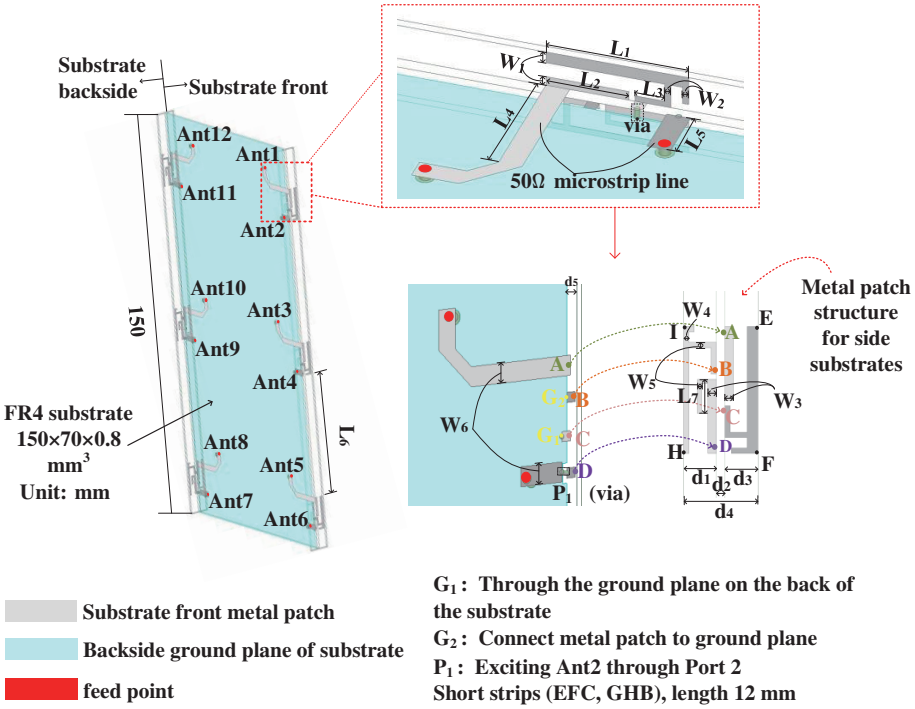

FIGURE 1. Geometry and detailed dimensions of the designed 12-port antenna.

TABLE 1. Dimensions of the single element.

Parameter	L_1	L_2	L_3	L_4	L_5	L_6	L_7	W_1	W_2
Value (mm)	12	7	2.5	12	5	42	5.2	1	0.5
Parameter	W_3	W_4	W_5	W_6	d_1	d_2	d_3	d_4	d_5
Value (mm)	0.8	0.5	0.4	2	3.1	0.8	3.1	7.0	1

2. ANTENNA STRUCTURE

Figure 1 illustrates the geometric configuration of a 12-element asymmetric mirror-coupled loop antenna, while Table 1 provides its detailed dimensions as a building block for MIMO operation in a smartphone. The two antennas (labeled as Ant1 and Ant2 in Fig. 1) are fabricated on the inner surface of a side frame encircling the perimeter of the system circuit board within the smartphone. To accommodate contemporary slim smartphone designs, the width of the side frame is intentionally limited to 7 mm. Each antenna's metal pattern on the side frame is oriented perpendicular to the system's ground plane, with an area of only $3.1 \times 12\,\text{mm}^2$ for each antenna. Ant1 and Ant2 are positioned on the front and back surfaces, respectively, in relation to the printed system ground plane on the system circuit board. A ground gap of 1 mm is between the metal patterns on the system ground plane and the frames of the two AM antennas.

The system circuit board measures $150 \times 75 \times 0.8\,\text{mm}^3$ tailored for a 5-inch smartphone. The side frames and system circuit boards are both manufactured using 0.8 mm thick FR-4 substrates with a relative dielectric constant of 4.4 and a loss tangent of 0.02. To supply Ant1 and Ant2, 50 Ω microstrip feedlines, 2 mm in width, are etched onto the system circuit board. A $12 \times 2\,\text{mm}^2$ feeder line is used for port 1 to excite Ant1, while a $5 \times 2\,\text{mm}^2$ feeder line is used for port 2 to excite Ant2.

Each antenna comprises a feed strip, a short-circuit strip, and a coupling gap, collectively forming a gap-coupled loop antenna. For Ant1, the feed strip measures 7 mm in length and 1 mm in width. The short-circuit strip (EFCG1 segment) spans a length of 17.6 mm, with a width of 1 mm for the EF segment and a length (L_1) of 12 mm. Point C is grounded to the system ground plane via a via at point G1. The coupling gap, positioned between the feed strip and the short-circuit strip section BC, boasts a width of 1.1 mm. For Ant2, in contrast to Ant1, an additional L-shaped stub measuring 5.2 mm in length is integrated into the feed strip. The short-circuit strip (HIBG2) extends over a length of 18.1 mm, with the HI segment width set at 0.5 mm. By modifying the width of the coupling gap, precise adjustments to the resonance frequency of the quarter-wave loop resonance mode can be achieved. Moreover, to supply Ant2, its feed strip links to the microstrip feedline on the front surface of the system circuit board via a via at P1. Notably, owing to the asymmetric design of Ant1 and Ant2, outstanding isolation is attained without the necessity of supplementary decoupling arrangements. This stems from the fact that when

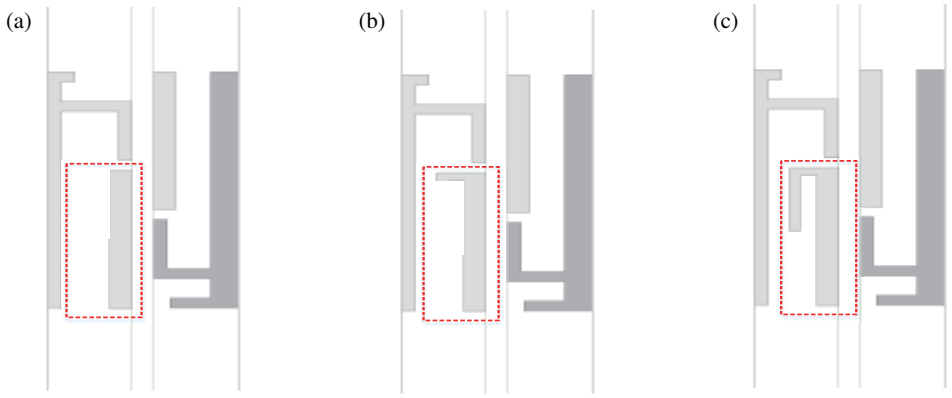

FIGURE 2. The evolution of the coupling gap zone.

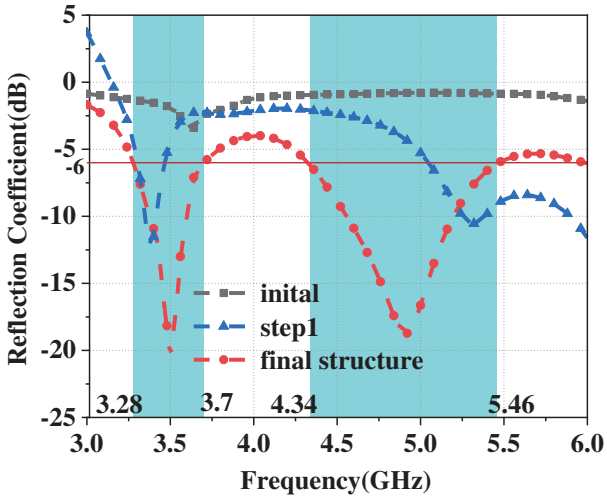

FIGURE 3. Reflection coefficient variation during antenna element design. (a) initial, (b) step 1, and (c) final structure.

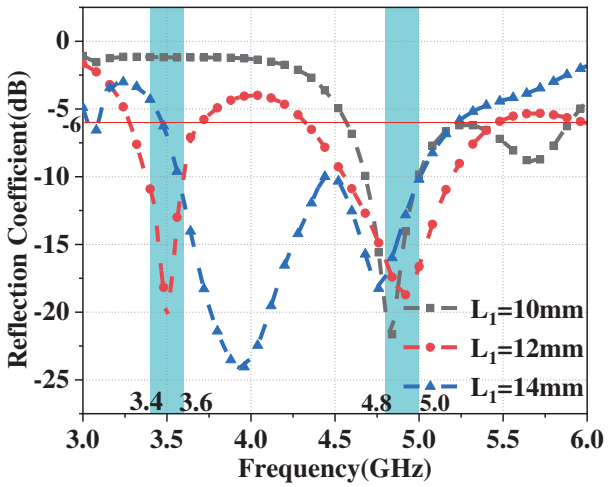

FIGURE 4. Effect of short-circuit band length L on reflection coefficient.

Ant1 is activated via port 1, a significant portion of the induced surface current on the system ground plane is directed towards the short-circuit strip (part HIBG2). In this scenario, the coupling gap between the short-circuit strip and the feed strip of Ant2 effectively obstructs the directed surface current from entering port 2. On the other hand, when Ant2 is stimulated via port 2, the coupling gap between the short-circuit strip and the feed strip of Ant1 hinders the directed surface current on the short-circuit strip from reaching port 1. Consequently, despite the typical absence of lateral spacing between the two asymmetric mirror (AM) antennas, the isolation between Ant1 and Ant2 can be augmented.

3. ANTENNA EVOLUTION PROCESS AND ANALYSIS

3.1. Evolution Process

In this design, a 50 Ω transmission feeding line and grounding plane are combined to investigate the impact of the individual antenna unit structure. Fig. 2 displays the evolution of the coupling gap for Ant2, while Fig. 3 illustrates the reflection coefficient characteristic curves associated with various coupling gap configurations within the same antenna unit (using Ant2 as a reference).

In the antenna structure depicted in Fig. 2(a), the coupling gap shape for Ant2 on the side baseplate is initially rectangular and serves for coupling feeding to Ant2, constituting the original design configuration of the antenna unit. As indicated by the initial curve in Fig. 3, when the antenna unit operates within the confines of the rectangular coupling gap, resonance mode is scarcely evident, and its impedance matching performance is notably deficient, with no discernible frequency bands available.

To extend the coverage of the designed antenna unit to the target frequency band, an I-shaped metal strip structure perpendicular to the side baseplate was incorporated into the original rectangular metal patch, as illustrated in Fig. 2(b). As indicated by the stp1 curve in Fig. 3, the addition of an I-shaped metal patch to the original coupling gap successfully altered the distribution of current on the metal plate, thereby enhancing the impedance matching performance of the unit and eliciting resonances at approximately 3.4 GHz and 4.3 GHz. Despite significant improvements in bandwidth and response frequency com-

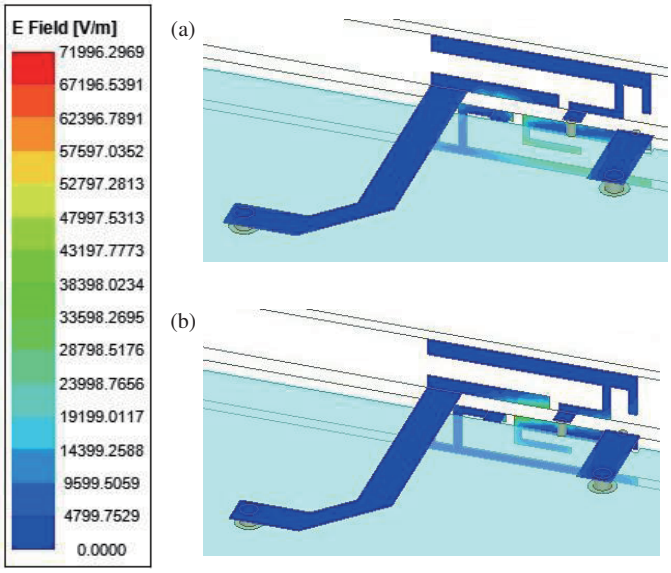

FIGURE 5. Surface current distribution of AM coupled building blocks in resonant mode. (a) 3.5 GHz; (b) 4.9 GHz.

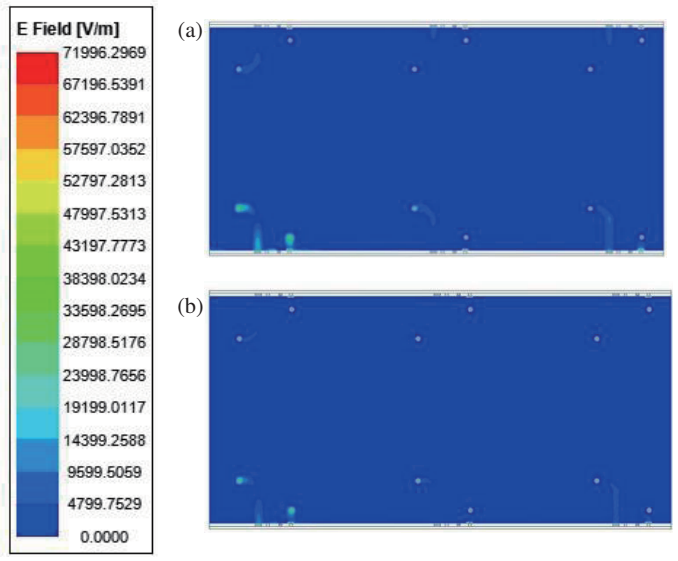

FIGURE 6. Current distribution of metal floor in resonant mode. (a) 3.5 GHz; (b) 4.9 GHz.

pared to the initial antenna structure, they still fell short of the desired frequency coverage.

To attain dual-band coverage, as depicted in Fig. 2(c), an additional length of 2.5 mm parallel to the side baseplate was appended to the metal patch, building upon the structure in Fig. 2(b). This introduced an L-shaped metal patch to the original rectangular coupling gap. As evidenced by the final structure curve in Fig. 3, adjusting the coupling gap shape led to a displacement of the original 4.3 GHz resonance point towards the higher frequencies, with a new resonance mode emerging at 4.9 GHz. This adjustment resulted in a further reduction in the reflection coefficient, reaching a minimum value of -18.7 dB, signifying enhanced impedance matching optimization. With a margin of -6 dB, it now spans 3.28–3.7 GHz and 4.34–5.46 GHz, thereby achieving comprehensive coverage of 5G bands.

3.2. Parameter Analysis

Parametric investigations were undertaken on the short-circuit strips (EFG1 and HIBG2 segments) of the antenna unit to explore the effects of varying lengths (L_1) of the EF and HI segments on the reflection coefficient. It is pertinent to note that throughout the study, while altering the length (L_1), the other dimensions of Ant1 and Ant2 remained constant. As depicted in Fig. 4, the findings suggest that with an increase in length (L_1), the resonance point at 3.4 GHz shifts towards higher frequencies. This phenomenon arises from the elongation of the short-circuit strip as the length (L_1) increases, consequently augmenting the overall resonant length of Ant1 and Ant2. In summary, adjusting the length (L_1) enables the antenna component to operate at the central frequency of the desired frequency band.

3.3. Current Distribution

To probe the operational mechanism of the antenna model proposed in this study, the current distribution of the individual antenna elements within the two modules was examined using the HFSS electromagnetic simulation software. Fig. 5 illustrates the current distribution on the patch surface of the asymmetric mirror (AM) building block in the resonance mode. As depicted in Fig. 5(a), during the 3.5 GHz resonance mode, the current on the antenna patch surface is predominantly concentrated in the lower half of the main system board. From Fig. 5(b), it is evident that at 4.9 GHz, the current distribution on the patch surface primarily clusters around the feed strip and gap-coupled strip of Ant1. Fig. 6 presents the comprehensive current distribution of the antenna when it is excited at 3.5 GHz and 4.9 GHz, respectively. It is discernible from the figures that when Ant1 is individually excited, the induced current from other antenna elements is negligible, suggesting minimal coupling effects.

4. RESULTS AND DISCUSSIONS

In this section, the feasibility of the proposed 12-element MIMO antenna system was investigated through fabrication and testing of the antenna model, as illustrated in Fig. 7. The discussion primarily revolves around the measured S-parameters, radiation characteristics, and efficiency of the MIMO antenna elements, alongside an analysis of MIMO performance through envelope correlation coefficient calculations. The 12-element asymmetric mirror-coupled loop MIMO antenna system was modeled and analyzed using electromagnetic simulation software HFSS, with the S-parameters of the fabricated prototype subsequently measured using a vector network analyzer. The feed patch is affixed to the inner core of the SMA connector, with the ground plane linked to the outer shell of the SMA connector. Throughout the testing phase,

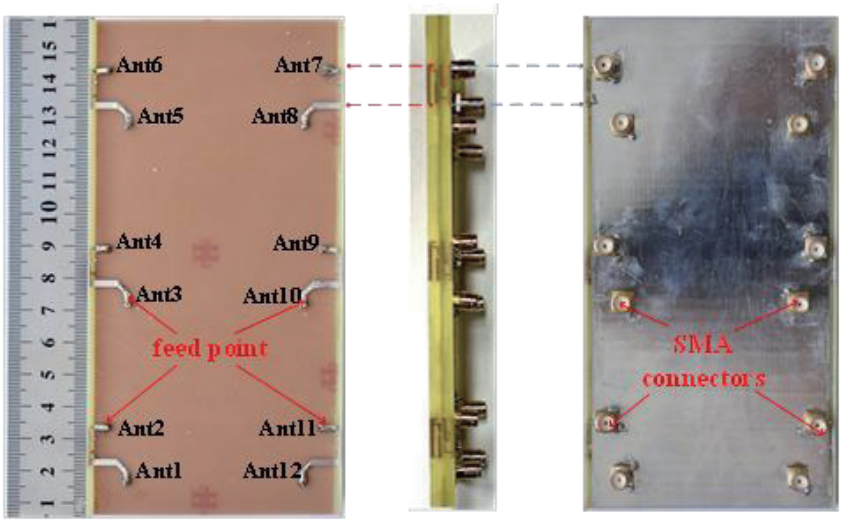

FIGURE 7. Manufactured antenna system.

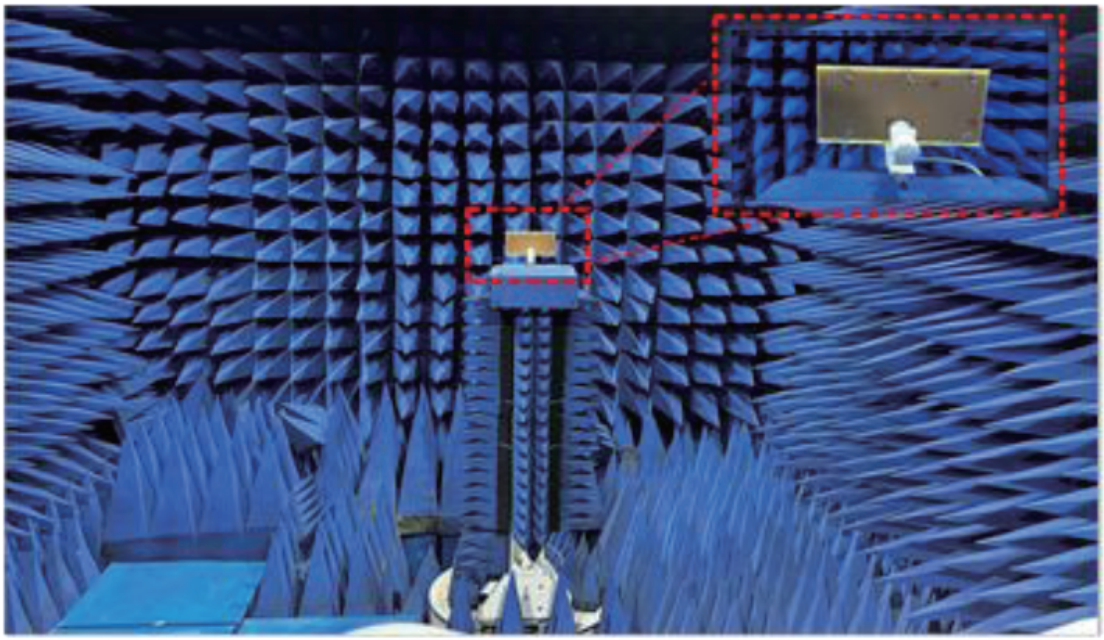

FIGURE 8. Far-field test environment.

the test port is linked to the cable, while the remaining ports necessitate matching to a 50 Ω load. The pertinent far-field measurements were conducted within a microwave anechoic chamber, as depicted in Fig. 8. Subsequent sections will introduce and analyze the corresponding results.

4.1. S-Parameters

Figures 9 and 10 present simulated and measured values, respectively, of the reflection coefficient and transmission coefficient for two antenna elements (Ant1 and Ant2) within the proposed 12-element antenna. In Fig. 9(a), the simulated reflection coefficient versus antenna frequency for the antenna elements is depicted. Notably, the reflection coefficients (S_{11} and S_{22}) for Ant1 and Ant2 remain below −10 dB across the desired frequency ranges of 3.4–3.6 GHz and 4.8–5.0 GHz, indicative of effective impedance matching. As shown in Fig. 10(a), the transmission coefficient S_{12} experiences a slight increase at 3.2 GHz but maintains isolation above 14.8 dB within the target operating frequency band. It is worth noting that although the measured isolation falls below −14 dB, it still meets the requirements of the antenna design. Analysis of the results in Fig. 9(b) and Fig. 10(b) reveals a close agreement between simulation and measurement. Discrepancies between simulated and measured outcomes may stem from losses in SMA connectors and transmission lines, or environmental factors during measurement.

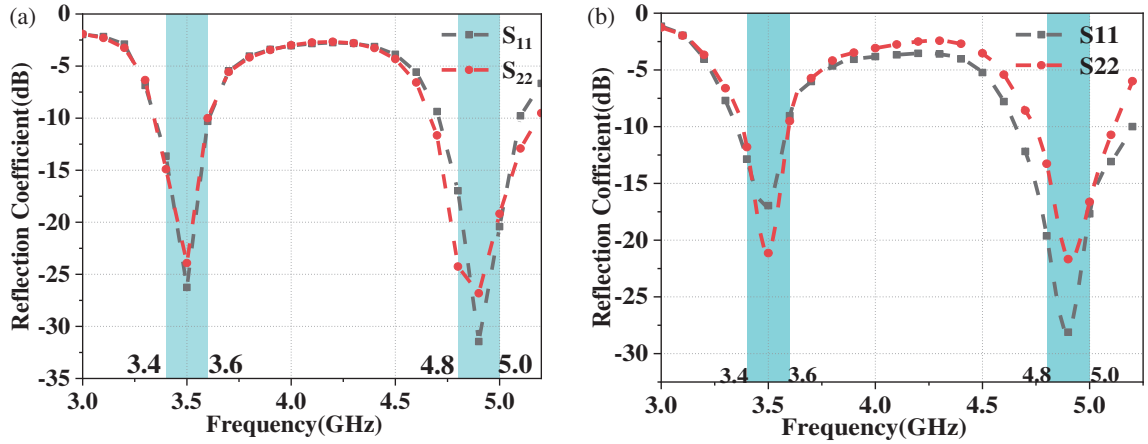

FIGURE 9. The results of reflection coefficients, (a) simulation; (b) measured.

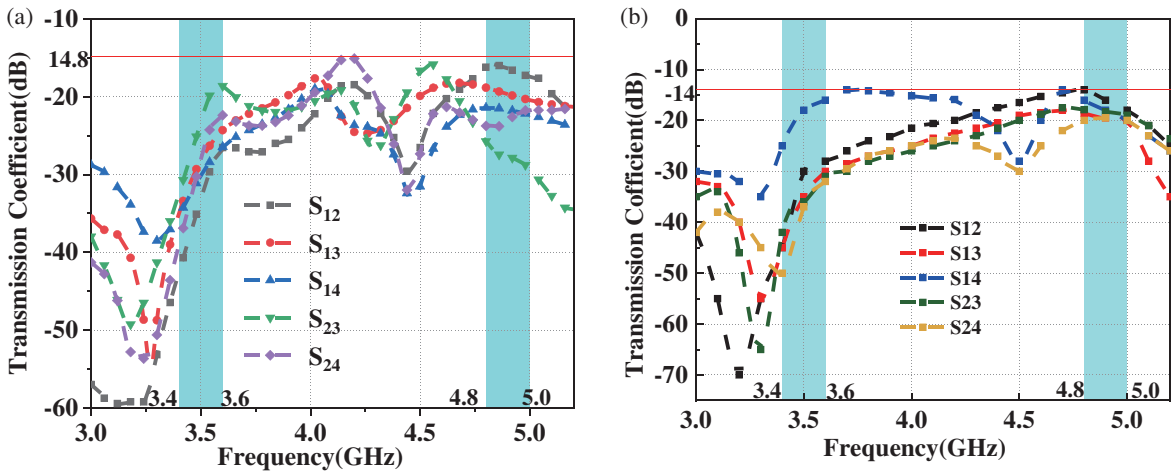

FIGURE 10. The results of transmission coefficients, (a) simulation; (b) measured.

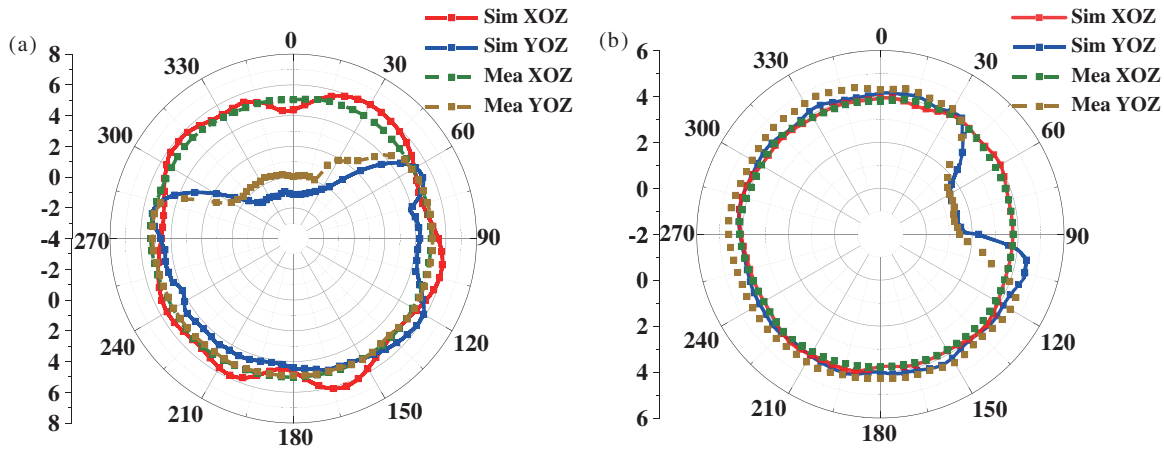

FIGURE 11. Simulated and measured 2D radiation patterns of the proposed MIMO system (a) Ant1 at 3.5 GHz; (b) Ant1 at 5.0 GHz.

4.2. Radiation Performance

Figure 11 illustrates the simulated and measured radiation patterns of the antenna element (with Ant1 as an example) when it is individually excited at different resonance modes in the XOZ and YOZ planes. It can be observed that at the resonance mode of 3.4 GHz, Ant1 demonstrates elevated radiation efficiency between 60° and 280° in the YOZ plane. At the resonance mode of 4.9 GHz, Ant1 exhibits higher radiation efficiency between 90° and −30° in the YOZ plane. On the other hand, Ant1 can effectively generate omnidirectional radiation

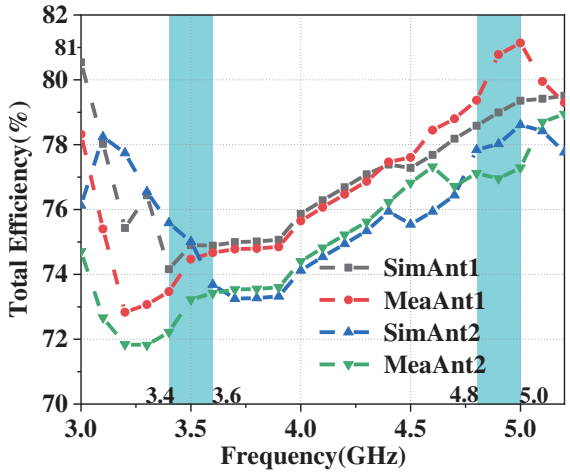

FIGURE 12. Simulated (Sim) and Measured (Mea) total efficiency values of Ant1 and Ant2.

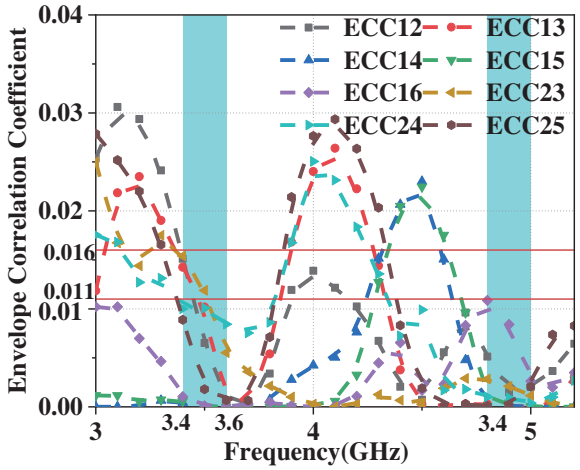

FIGURE 13. Envelope correlation coefficients of MIMO antenna elements.

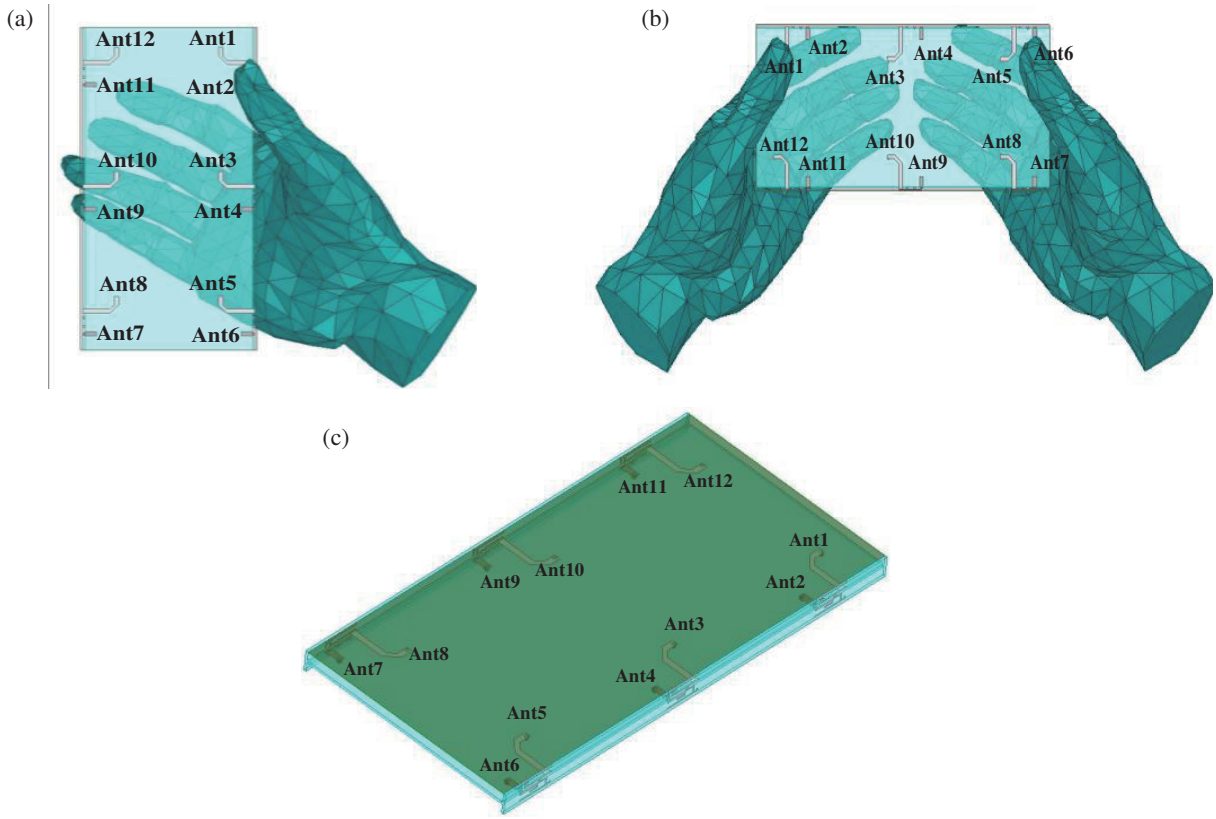

FIGURE 14. Two application scenarios of handheld smart phones. (a) SHM; (b) DHM; (c) Overlay Screen.

in the XOZ radiation plane. Owing to the mirrored distribution of antenna elements, the radiation directions of the antennas complement each other, thereby engendering exceptional far-field radiation characteristics.

Figure 12 presents the total efficiency obtained from simulation and measurement. It is evident that in the 3.4 GHz frequency band, the simulated and measured efficiencies of the antenna range from 72% to 75%, whereas within the 4.9 GHz frequency band, the simulated and measured efficiencies span from 77% to 81%. In conclusion, the proposed 12-element MIMO antenna system has high radiation efficiency.

4.3. Envelope Correlation Coefficient

The envelope correlation coefficient (ECC) serves as a vital metric for characterizing MIMO antenna correlation quality. A lower ECC value signifies superior MIMO system performance, as it correlates with reduced levels of mutual coupling

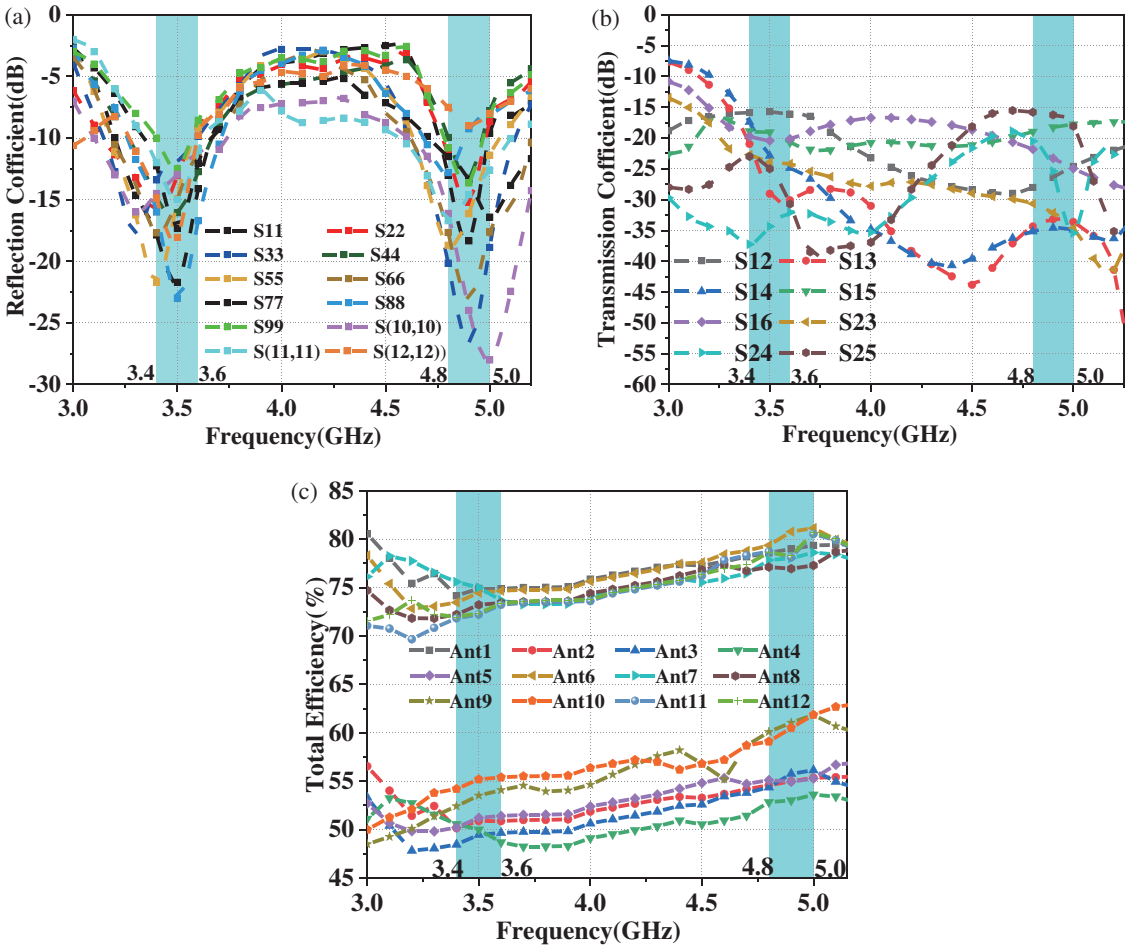

FIGURE 15. Simulated performance parameters in SHM mode, (a) reflection coefficient (b) transmission coefficient (c) total efficiency.

and diminished influence of each antenna on others when operating independently. As illustrated in Fig. 13, within the 3.4 GHz frequency band (3.3–3.6 GHz), the ECC value remains below 0.016, while within the 4.9 GHz frequency band (4.8–5.0 GHz), the ECC value is a mere 0.011. Based on the comprehensive ECC simulation results, the antenna structure proposed in this paper demonstrates commendable diversity performance. The ECC can be computed from the S-parameter using the following equation:

$$\mathrm{ECC}_{ij} = \frac{\left|S_{ii}^{*}S_{ij}+S_{ji}^{*}S_{jj}\right|^{2}}{\left(1-\left|S_{ii}\right|^{2}-\left|S_{ji}\right|^{2}\right)\left(1-\left|S_{jj}\right|^{2}-\left|S_{ij}\right|^{2}\right)} \quad (1)$$

5. PRACTICAL APPLICATION ANALYSIS

This section will investigate the influence of the common single-hand mode (SHM), double-hand mode (DHM), and overlay screen mode on antenna performance. The SHM, DHM, and overlay screen mode are illustrated in Fig. 14, while Figs. 15, 16, and 17 provide the simulated results of the performance under these three scenarios.

Figure 15(a) reveals that contact with fingers causes the resonant frequencies of Ant2, Ant3, Ant4, Ant5, Ant9, and Ant10 to shift, resulting in degraded impedance matching, albeit still covering the desired frequency band. As depicted in Fig. 15(b), the transmission coefficient between antennas decreases due to finger or palm obstruction, indicating that some electromagnetic waves are absorbed by body tissue, elevating the isolation between antennas to 15 dB. Fig. 15(c) presents the antenna efficiency after incorporating a hand model, showing reduced efficiency (about 25%) for antenna elements near fingers, yet still meeting 5G communication requirements.

Similarly, Fig. 16 demonstrates that Ant1, Ant6, Ant7, Ant11, and Ant12, situated near the hand structure experience resonant frequency shifts, increased isolation, and decreased efficiency. However, the efficiency for all antennas remains above 45%. As shown in Fig. 17, the addition of a mobile phone screen results in a slight shift in the resonant frequency of the antenna, while maintaining a high isolation between antenna elements, and the efficiency of all antennas remains above 40%. In summary, the MIMO antenna maintains commendable performance and exhibits high interference

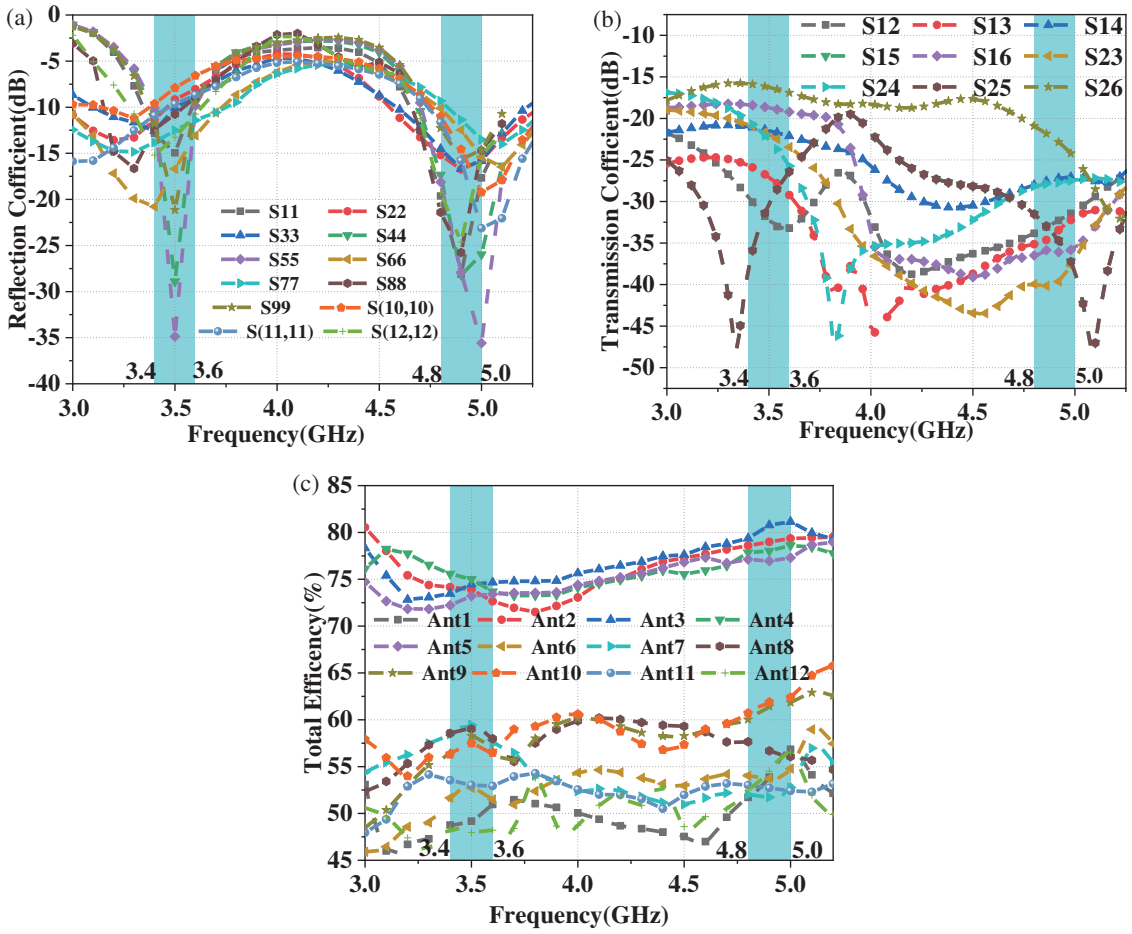

FIGURE 16. Simulated performance parameters in DHM mode, (a) reflection coefficient (b) transmission coefficient (c) efficiency.

TABLE 2. Performance comparison of the proposed MIMO antenna with other works.

References	bands (GHz)	Isolatio (dB)	ECC	Total Efficiency (%)
[11]	3.23–5.41	>15		48–70
[17]	3.4–3.6	>12	<0.02	60–90
[21]	3.4–3.6	>16.7	<0.1	54–65
[33]	3.3–3.7, 4.85–5.08	>12		30–60
[34]	3.3–4.2	>9.5	<0.06	40–58
[35]	3.3–4.2, 4.4–5.0	>11.5	<0.2	38–52
[36]	3.4–3.6	>16.7	<0.1	54–65
Proposed	3.3–3.6, 4.8–5.0	>14	<0.016	72–81

resistance under both single-hand and double-hand operational modes.

6. MIMO ANTENNA PERFORMANCE COMPARISON

To further illustrate the characteristics of the proposed MIMO antenna system, Table 2 compares the performance of the designed MIMO antenna system with some reference antenna systems proposed in other literatures. Based on the design specifications for MIMO antennas, the comparison is mainly focused on four aspects: bandwidth, isolation, efficiency, and ECC. From the table, it can be observed that the advantages of the designed antenna array are mainly as follows: by increasing the number of antennas, it ensures that the isolation is greater than 14 dB within a limited spatial layout. The MIMO antenna designed in this paper can cover the frequency bands

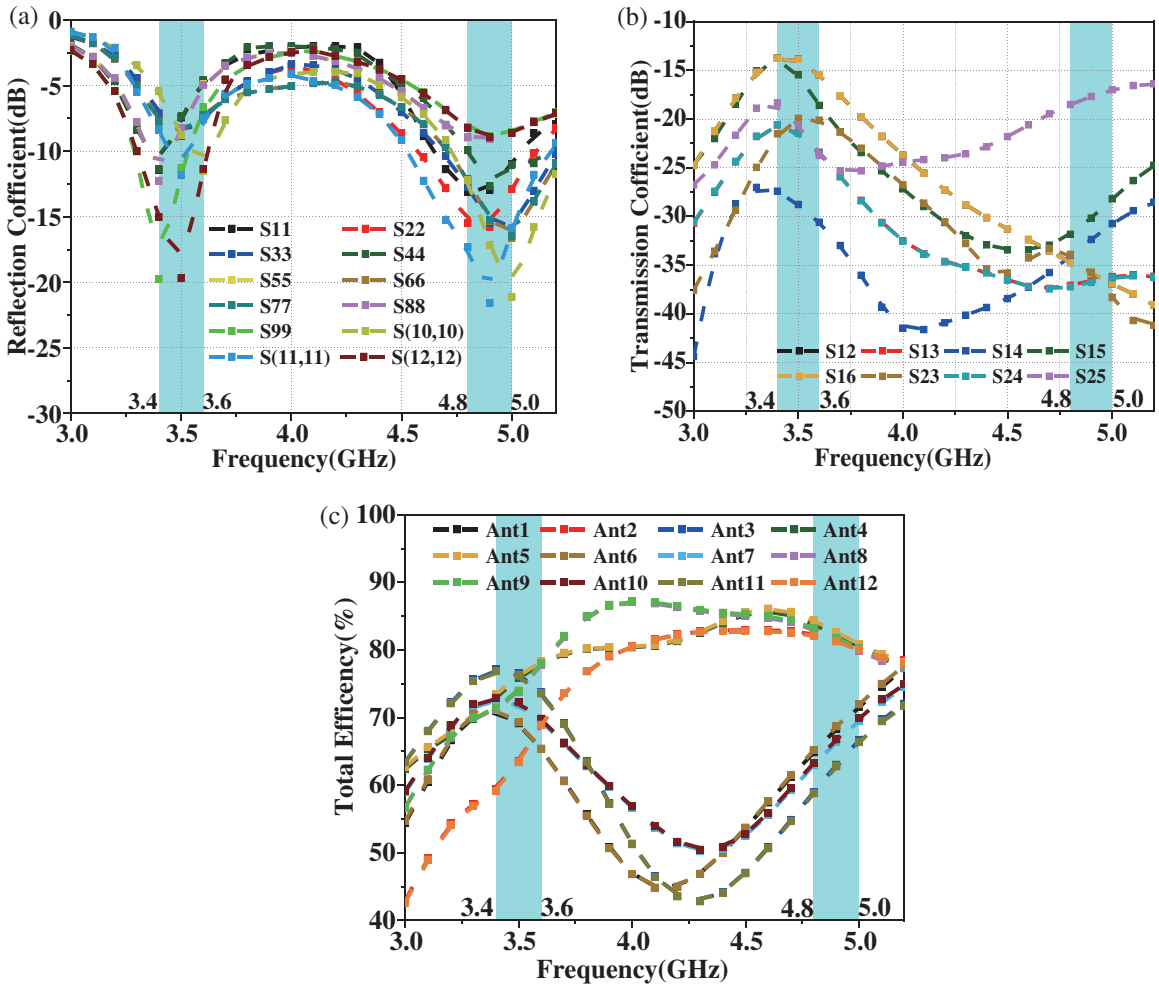

FIGURE 17. Simulated performance parameters under overlay screen mode, (a) reflection coefficient (b) transmission coefficient (c) efficiency.

of 3.3–3.6 GHz and 4.8–5.0 GHz, achieving dual-band coverage. In terms of isolation, the designed antenna in this paper exhibits superior isolation compared to the antennas in references [17, 33–35]. Moreover, in terms of ECC and efficiency, the designed antenna also demonstrates significant advantages compared to the antennas in [11, 17, 21, 33–36]. Additionally, the asymmetric mirror-coupled loop antenna employed in this section is used to form two resonance modes at 3.5 GHz and 4.9 GHz. The antenna does not need additionally decoupling elements, which achieves excellent isolation based on its own structural advantages, showcasing a certain level of innovation. The designed MIMO antenna array has passed simulated testing, and the results meet the design requirements for MIMO antennas, making it suitable for 5G communications.

7. CONCLUSIONS

This paper introduces a 12-element asymmetric mirror-coupled loop antenna designed for 5G smartphones. Comprising six identical AM coupled building blocks, each housing two gap-coupled loop antennas, and the antenna exhibits an asymmetric mirror (AM) structure relative to the smartphone's ground plane, with each block measuring a mere $12 \times 7\,\text{mm}^2$. Leveraging this unique design, the proposed antenna achieves an isolation exceeding 14 dB without the need for additional decoupling structures, effectively covering the dual band 5G frequency ranges of 3.3–3.6 GHz and 4.8–5.0 GHz. Optimization of the antenna design was conducted using HFSS simulation software, yielding an envelope correlation coefficient below 0.08 and an efficiency range of 72%–81%. Upon fabrication, the prototype was subjected to measurement, demonstrating consistency with simulated results within the margin of error. Furthermore, the impact of user interaction on handset smartphones was explored. Based on these findings, the proposed 12-element MIMO antenna holds significant promise for 5G smartphone applications.

ACKNOWLEDGEMENT

This work was supported in part by the Natural Science Research Project of Anhui Educational Committee under No. 2022AH051583 and No. 2022AH052138, in part by the Anhui Province Graduate Academic Innovation Project under grant No. 2023xscx074.

REFERENCES

[1] Yuan, X.-T., Z. Chen, T. Gu, and T. Yuan, "A wideband PIFA-pair-based MIMO antenna for 5G smartphones," *IEEE Antennas and Wireless Propagation Letters*, Vol. 20, No. 3, 371–375, 2021.

[2] Serghiou, D., M. Khalily, V. Singh, A. Araghi, and R. Tafazolli, "Sub-6 GHz dual-band 8×8 MIMO antenna for 5G smartphones," *IEEE Antennas and Wireless Propagation Letters*, Vol. 19, No. 9, 1546–1550, 2020.

[3] Yuan, X.-T., W. He, K.-D. Hong, C.-Z. Han, Z. Chen, and T. Yuan, "Ultra-wideband MIMO antenna system with high element-isolation for 5G smartphone application," *IEEE Access*, Vol. 8, 56 281–56 289, 2020.

[4] Zhao, A. and Z. Ren, "Wideband MIMO antenna systems based on coupled-loop antenna for 5G N77/N78/N79 applications in mobile terminals," *IEEE Access*, Vol. 7, 93 761–93 771, 2019.

[5] Wang, H., R. Zhang, Y. Luo, and G. Yang, "Design of MIMO antenna system operating in wideband of 3300 to 6400 MHz for future 5G mobile terminal applications," *International Journal of RF and Microwave Computer-Aided Engineering*, Vol. 30, No. 12, e22426, 2020.

[6] Huang, J., T. He, S. Xi, Q. Yang, X. Shi, and G. Liu, "Eight-port high-isolation antenna array for 3.3-6 GHz handset applications," *AEU — International Journal of Electronics and Communications*, Vol. 154, 154333, 2022.

[7] Ren, Z., A. Zhao, and S. Wu, "Dual-band MIMO antenna system for 5G mobile terminals," in *2019 13th European Conference on Antennas and Propagation (EuCAP)*, 1–4, Krakow, Poland, 2019.

[8] Li, J., X. Zhang, Z. Wang, X. Chen, J. Chen, Y. Li, and A. Zhang, "Dual-band eight-antenna array design for MIMO applications in 5G mobile terminals," *IEEE Access*, Vol. 7, 71 636–71 644, 2019.

[9] Yuan, X.-T., Z. Chen, J. Li, and T. Yuan, "A compact dual-band and high-isolation MIMO antenna system for 5G smartphone applications," in *2020 IEEE MTT-S International Microwave Workshop Series on Advanced Materials and Processes for RF and THz Applications (IMWS-AMP)*, 1–3, Suzhou, China, 2020.

[10] Jiang, W., Y. Cui, B. Liu, W. Hu, and Y. Xi, "A dual-band MIMO antenna with enhanced isolation for 5G smartphone applications," *IEEE Access*, Vol. 7, 112 554–112 563, 2019.

[11] Su, H.-L. and C.-L. Tsao, "A sub-6 GHz 8×8 MIMO antenna array for 5G mobile phone applications," in *2023 IEEE International Symposium On Antennas And Propagation (ISAP)*, 1–2, Kuala Lumpur, Malaysia, 2023.

[12] Sun, L., Y. Li, and Z. Zhang, "Wideband integrated quad-element MIMO antennas based on complementary antenna pairs for 5G smartphones," *IEEE Transactions on Antennas and Propagation*, Vol. 69, No. 8, 4466–4474, 2021.

[13] Kiani, S. H., M. E. Munir, H. S. Savci, H. Rimli, E. Alabdulkreem, H. Elmannai, G. Pau, and M. Alibakhshikenari, "Dual-polarized wideband 5G N77 band slotted MIMO antenna system for next-generation smartphones," *IEEE Access*, Vol. 12, 34 467–34 476, 2024.

[14] Hu, W., Z. Chen, L. Qian, L. Wen, Q. Luo, R. Xu, W. Jiang, and S. Gao, "Wideband back-cover antenna design using dual characteristic modes with high isolation for 5G MIMO smartphone," *IEEE Transactions on Antennas and Propagation*, Vol. 70, No. 7, 5254–5265, 2022.

[15] Padmanathan, S., A. A. Al-Hadi, A. M. Elshirkasi, S. S. Al-Bawri, M. T. Islam, T. Sabapathy, M. Jusoh, P. Akkaraekthalin, and P. J. Soh, "Compact multiband reconfigurable MIMO antenna for sub-6 GHz 5G mobile terminal," *IEEE Access*, Vol. 10, 60 241–60 252, 2022.

[16] Jaglan, N., S. D. Gupta, B. K. Kanaujia, and M. S. Sharawi, "10 element sub-6-GHz multi-band double-T based MIMO antenna system for 5G smartphones," *IEEE Access*, Vol. 9, 118 662–118 672, 2021.

[17] Ullah, R., S. Ullah, R. Ullah, F. Faisal, I. B. Mabrouk, and M. J. A. Hasan, "A 10-ports MIMO antenna system for 5G smartphone applications," *IEEE Access*, Vol. 8, 218 477–218 488, 2020.

[18] Al-Hadi, A. A., J. Ilvonen, R. Valkonen, and V. Viikari, "Eight-element antenna array for diversity and MIMO mobile terminal in LTE 3500 MHz band," *Microwave and Optical Technology Letters*, Vol. 56, No. 6, 1323–1327, 2014.

[19] Jiang, W., Y. Cui, B. Liu, W. Hu, and Y. Xi, "A dual-band MIMO antenna with enhanced isolation for 5G smartphone applications," *IEEE Access*, Vol. 7, 112 554–112 563, 2019.

[20] Li, M.-Y., Z.-Q. Xu, Y.-L. Ban, C.-Y.-D. Sim, and Z.-F. Yu, "Eight-port orthogonally dual-polarised MIMO antennas using loop structures for 5G smartphone," *IET Microwaves, Antennas & Propagation*, Vol. 11, No. 12, 1810–1816, 2017.

[21] Fang, Y., Y. Jia, J.-Q. Zhu, Y. Liu, and J. An, "Self-decoupling, shared-aperture, eight-antenna MIMO array with MIMO-SAR reduction," *IEEE Transactions on Antennas and Propagation*, Vol. 72, No. 2, 1905–1910, 2024.

[22] Moses, A. T. Z. and N. Moses, "Compact self decoupled MIMO antenna pairs covering 3.4–3.6 GHz band for 5G handheld device applications," *AEU — International Journal of Electronics and Communications*, Vol. 141, 153971, 2021.

[23] Xu, H., S. S. Gao, H. Zhou, H. Wang, and Y. Cheng, "A highly integrated MIMO antenna unit: Differential/common mode design," *IEEE Transactions on Antennas and Propagation*, Vol. 67, No. 11, 6724–6734, 2019.

[24] Sun, L., Y. Li, Z. Zhang, and Z. Feng, "Wideband 5G MIMO antenna with integrated orthogonal-mode dual-antenna pairs for metal-rimmed smartphones," *IEEE Transactions on Antennas and Propagation*, Vol. 68, No. 4, 2494–2503, 2020.

[25] Han, C.-Z., L. Xiao, Z. Chen, and T. Yuan, "Co-located self-neutralized handset antenna pairs with complementary radiation patterns for 5G MIMO applications," *IEEE Access*, Vol. 8, 73 151–73 163, 2020.

[26] Chang, L., Y. Yu, K. Wei, and H. Wang, "Polarization-orthogonal co-frequency dual antenna pair suitable for 5G MIMO smartphone with metallic bezels," *IEEE Transactions on Antennas and Propagation*, Vol. 67, No. 8, 5212–5220, 2019.

[27] Li, M.-Y., Z.-Q. Xu, Y.-L. Ban, C.-Y.-D. Sim, and Z.-F. Yu, "Eight-port orthogonally dual-polarised MIMO antennas using loop structures for 5G smartphone," *IET Microwaves, Antennas & Propagation*, Vol. 11, No. 12, 1810–1816, 2017.

[28] Sun, L., H. Feng, Y. Li, and Z. Zhang, "Compact 5G MIMO mobile phone antennas with tightly arranged orthogonal-mode pairs," *IEEE Transactions on Antennas and Propagation*, Vol. 66, No. 11, 6364–6369, 2018.

[29] Ye, Y., X. Zhao, and J. Wang, "Compact high-isolated MIMO antenna module with chip capacitive decoupler for 5G mobile terminals," *IEEE Antennas and Wireless Propagation Letters*, Vol. 21, No. 5, 928–932, 2022.

[30] Yang, B., Y. Xu, J. Tong, Y. Zhang, Y. Feng, and Y. Hu, "Tri-port antenna with shared radiator and self-decoupling characteristic for 5G smartphone application," *IEEE Transactions on Antennas and Propagation*, Vol. 70, No. 6, 4836–4841, 2022.

[31] Subbaraj, S., M. Kanagasabai, P. Sambandam, M. G. N. Alsath, S. K. Palaniswamy, and S. Kingsly, "Performance enhanced folded multiband MIMO antenna for mobile terminals," *AEU —*

International Journal of Electronics and Communications, Vol. 137, 153750, 2021.

[32] Blanch, S., J. Romeu, and I. Corbella, "Exact representation of antenna system diversity performance from input parameter description," *Electronics Letters*, Vol. 39, No. 9, 705–707, 2003.

[33] Zhang, W., Z. Weng, and L. Wang, "Design of a dual-band MIMO antenna for 5G smartphone application," in *2018 International Workshop on Antenna Technology (iWAT)*, 1–3, 2018.

[34] Barani, I. R. R., K.-L. Wong, Y.-X. Zhang, and W.-Y. Li, "Low-profile wideband conjoined open-slot antennas fed by grounded coplanar waveguides for 4×4 5G MIMO operation," *IEEE Transactions on Antennas and Propagation*, Vol. 68, No. 4, 2646–2657, 2020.

[35] Ahn, J., Y. Youn, B. Kim, J. Lee, N. Choi, Y. Lee, G. Kim, and W. Hong, "Wideband 5G N77/N79 4×4 MIMO antenna featuring open and closed stubs for metal-rimmed smartphones with four slits," *IEEE Antennas and Wireless Propagation Letters*, Vol. 22, No. 12, 2798–2802, 2023.

[36] Fang, Y., Y. Jia, J.-Q. Zhu, Y. Liu, and J. An, "Self-decoupling, shared-aperture, eight-antenna MIMO array with MIMO-SAR reduction," *IEEE Transactions on Antennas and Propagation*, Vol. 72, No. 2, 1905–1910, 2024.